

Halo shapes constrained from a pure sample of central galaxies in KiDS-1000

Christos Georgiou^{1*}, Henk Hoekstra¹, Konrad Kuijken¹, Maciej Bilicki², Andrej Dvornik³, Thomas Erben⁴, Benjamin Giblin⁵, Catherine Heymans^{3,5}, Hendrik Hildebrandt³, Jelte T. A. de Jong⁶, Arun Kannawadi^{1,7}, Peter Schneider⁴, Tim Schrabback⁴, HuanYuan Shan^{8,9}, and Angus H. Wright³

¹ Leiden Observatory, Leiden University, Niels Bohrweg 2, 2333 CA, Leiden, The Netherlands.

² Center for Theoretical Physics, Polish Academy of Sciences, al. Lotników 32/46, 02-668, Warsaw, Poland.

³ Ruhr University Bochum, Faculty of Physics and Astronomy, Astronomical Institute (AIRUB), German Centre for Cosmological Lensing, 44780 Bochum, Germany

⁴ Argelander-Institut für Astronomie, Universität Bonn, Auf dem Hügel 71, 53121, Bonn, Germany.

⁵ Institute for Astronomy, University of Edinburgh, Royal Observatory, Blackford Hill, Edinburgh, EH9 3HJ, UK

⁶ Kapteyn Astronomical Institute, University of Groningen, PO Box 800, 9700 AV Groningen, the Netherlands

⁷ Department of Astrophysical Sciences, Princeton University, 4 Ivy Lane, Princeton, NJ 08544, USA

⁸ Shanghai Astronomical Observatory (SHAO), Nandan Road 80, Shanghai 200030, China

⁹ University of Chinese Academy of Sciences, Beijing 100049, China

Received <date> / Accepted <date>

ABSTRACT

We present measurements of f_h , the ratio of the aligned components of the projected halo and galaxy ellipticities, for a sample of central galaxies using weak gravitational lensing data from the Kilo-Degree Survey (KiDS). Using a lens galaxy shape estimation that is more sensitive to outer galaxy regions, we find $f_h = 0.50 \pm 0.20$ for our full sample and $f_h = 0.55 \pm 0.19$ for an intrinsically red (and therefore higher stellar-mass) sub-sample, rejecting the hypothesis of round halos and/or galaxies being un-aligned with their parent halo at 2.5σ and 2.9σ , respectively. We quantify the 93.4% purity of our central galaxy sample using numerical simulations and overlapping spectroscopy from the Galaxy and Mass Assembly survey. This purity ensures that the interpretation of our measurements is not complicated by the presence of a significant fraction of satellite galaxies. Restricting our central galaxy ellipticity measurement to the inner isophotes, we find $f_h = 0.34 \pm 0.17$ for our red sub-sample, suggesting that the outer galaxy regions are more aligned with their dark matter halos compared to the inner regions. Our results are in agreement with previous studies and suggest that lower mass halos are rounder and/or less aligned with their host galaxy than samples of more massive galaxies, studied in galaxy groups and clusters.

Key words. Gravitational lensing: weak - galaxies: general

1. Introduction

The current standard model of cosmology, dubbed Λ CDM, has been very successful in describing a large number of independent cosmological probes, such as Cosmic Microwave Background (CMB) observations (e.g. Planck Collaboration et al. 2020), the galaxy clustering signal (e.g. Alam et al. 2017) and Baryon Acoustic Oscillations (e.g. Anderson et al. 2014; Bautista et al. 2018), among many others. According to this model, dark matter makes up for the majority of the matter density content of the Universe and provides the seeds upon which galaxies and larger structures can form and evolve.

From numerical simulations, it is understood that dark matter forms halos that are roughly tri-axial, which appear elliptical in projection (Dubinski & Carlberg 1991; Jing & Suto 2002). Estimation of the shape of these halos from observations can, therefore, be used as a test for the current cosmological model, as well as extensions to it, such as modifications to the gravity theory or the dark matter component (e.g. Hellwing et al. 2013; L'Huillier et al. 2017; Peter et al. 2013; Elahi et al. 2014).

Observationally, many attempts have been made towards measuring halo ellipticities. Techniques include satellite dynamics (e.g. Brainerd 2005; Azzaro et al. 2007; Bailin et al. 2008; Nierenberg et al. 2011), tidal streams in the Milky Way (e.g. Helmi 2004; Law & Majewski 2010; Vera-Ciro & Helmi 2013), HI gas observations (e.g. Olling 1995; Banerjee & Jog 2008; O'Brien et al. 2010), planetary nebulae (e.g. Hui et al. 1995; Napolitano et al. 2011), X-ray observations (e.g. Donahue et al. 2016) as well as strong lensing (e.g. Caminha et al. 2016), also accompanied by stellar dynamics (e.g. van de Ven et al. 2010). These techniques rely on luminous tracers of the dark matter shape, which can lead to biases, complicate the interpretation of the measurements and cannot provide information on the larger scales of the dark matter halo, where visible light is absent.

One observational technique that does not suffer from this drawback is weak gravitational lensing, the coherent distortion of light rays from background sources from the intervening matter distribution (for a review, see Bartelmann & Schneider 2001). Since gravitational lensing is sensitive to all matter (also non-baryonic), it serves as a great tool to study the dark matter halos. The distortion of the galaxy shapes due to weak lensing is very small, and in order to extract a measurable signal one

* georgiou@strw.leidenuniv.nl

needs to statistically average over large ensembles of galaxies. If the stacking is done around other galaxies, a technique called galaxy-galaxy lensing, only the matter at the lens galaxy redshift contributes coherently to the lensing signal, and the structures along the line of sight simply add noise to the measurement.

Tri-axial dark matter halos will cause an azimuthal variation in the weak lensing signal, enhancing it along the direction of the semi-major axis of the projected halo and reducing it along the semi-minor axis. For very massive structures, such as large galaxy clusters, this variation is strong enough to be measured for individual (e.g. Corless et al. 2009; Umetsu et al. 2018) or stacked weak lensing maps of cluster samples (Evans & Bridle 2009; Oguri et al. 2012). For galaxy-scale halos, this variation can be measured by weighting the lensing measurements according to the halo's semi-major axis.

In most applications of weak lensing based measurements of dark matter halo ellipticity, the lens galaxy semi-major axis is used as a proxy for the dark matter halo axis (Hoekstra et al. 2004; Mandelbaum et al. 2006; Parker et al. 2007; van Uitert et al. 2012; Schrabback et al. 2015; van Uitert et al. 2017; Schrabback et al. 2020). The measured quantity is, then, the ratio of the halo ellipticity to the galaxy ellipticity, weighted by the average mis-alignment angle between the two, i.e. $f_h = \langle \cos(2\Delta\phi_{h,g}) |\epsilon_h|/|\epsilon_g| \rangle$. This makes the measurement of f_h a useful step in determining the alignment between the dark matter halo and its host galaxy. The mis-alignment angle has been measured in numerical simulations, with results from the most recent hydrodynamical simulations suggesting a value of $\langle \Delta\phi_{h,g} \rangle \sim 30^\circ$ (Tenneti et al. 2014; Velliscig et al. 2015; Chisari et al. 2017). The mis-alignment is decreasing with decreasing redshift and increasing halo mass, which suggests that massive central galaxies are expected to carry most of the signal. Indeed van Uitert et al. (2017) detected a non-zero halo ellipticity with $\gtrsim 3\sigma$ significance using only ~ 2500 lenses. These lenses were confirmed central galaxies of a galaxy group from a friends-of-friends-based group catalogue built using spectroscopic data.

Motivated by this, we aim to define a sample of central galaxies with very high purity from a *photometric* galaxy sample, and use these as lenses to measure the anisotropic weak lensing signal around them. A galaxy sample with low satellite fraction will also produce a more robust measurement, since satellite galaxy lensing profiles across a wide range of scales complicate the interpretation of the measured signal of the full sample. We use the fourth data release of the Kilo-Degree-Survey (KiDS, Kuijken et al. 2019) and construct an algorithm that preferentially selects central galaxies using apparent magnitudes and photometric redshifts. These redshifts are obtained from a machine learning technique, focussing on the bright-end sample of galaxies in KiDS, and achieve very high precision (Bilicki et al. 2018). We validate our central galaxy selection by quantifying the sample's purity using the group catalogue from the Galaxy And Mass Assembly survey (GAMA, Driver et al. 2011; Robotham et al. 2011), as well as mock galaxy catalogues from the Marenstrum Institut de Ciències de l'Espai (MICE) Grand Challenge run (Crocce et al. 2015).

In Sect. 2 we present the data used for constructing and validating our lens sample, consisting of highly pure central galaxies, which we describe in detail in Sect. 3. The methodology used to measure the lensing signal is described in Sect. 4. The results obtained are shown in Sect. 5 and we discuss the measurements and conclude with Sect. 6. To calculate angular diameter distances we use a flat Λ CDM cosmology with parameters obtained from the latest CMB constraints (Planck Collaboration et al. 2020), i.e. $H_0 = 67.4$ km/s/Mpc and $\Omega_{m,0} = 0.313$.

2. Data

Measuring the anisotropic lensing signal requires a wide survey of deep imaging data, so that accurate unbiased galaxy shapes can be measured and the lensing signal can be statistically extracted. For this reason, we use data from KiDS. Moreover, massive central galaxies are expected to yield the highest signal-to-noise ratio (SNR) for anisotropic lensing; we thus need a way of selecting a pure sample of central galaxies as well as a means to validate our selection. To this end, we make use of the GAMA survey, as well as mock catalogues from the MICE Grand Challenge galaxy catalogue.

2.1. KiDS-1000

KiDS¹ (de Jong et al. 2015, 2017; Kuijken et al. 2019) is a deep imaging ESO public survey carried out using the VLT Survey Telescope and the OmegaCam camera. The survey has covered 1,350 deg² of the sky in three patches in the northern and southern equatorial hemispheres, in four broad band filters (u , g , r and i). The mean limiting magnitudes are 24.23, 25.12, 25.02 and 23.68, for the four filters respectively (5σ in a 2'' aperture). The survey was specifically designed for weak lensing science and the image quality is high, with small nearly round point-spread function (PSF), especially in the r -band observations, which were taken during dark time with the best seeing conditions. We use the fourth data release of the survey, with 1006 1×1 deg² image tiles (KiDS-1000).

KiDS is complemented by the VISTA Kilo-Degree Infrared Galaxy Survey (VIKING, Edge et al. 2013), which has imaged the same footprint as KiDS in the near-infrared (NIR) Z , Y , J , H and K_s bands. This addition allows for the determination of more accurate photometric redshifts from 9 broad band filters. For our source galaxy sample, redshifts are retrieved with the template fitting Bayesian Photometric Redshift (BPZ) code (Benítez 2000; Coe et al. 2006), applied to the 9 band photometry. To estimate source redshift distributions, we use the direct calibration scheme to weight the overlapping spectroscopic sample according to our photometric one. The process is described in detail in Hildebrandt et al. (2020).

For our lens sample, we require more precise redshift estimates that will help in a more accurate lensing measurement, as well as in building a more robust central galaxy sample. Hence, we choose to use a bright ($m_r \lesssim 20$) sample with photometric redshifts estimated with the artificial neural network machine learning code ANNz2 (Sadeh et al. 2016), as presented in Bilicki et al. (2018), but now extended to the full KiDS-1000 sample (Bilicki et al. 2021). This sample was trained on the highly complete GAMA spectroscopic redshift catalogue (98.5% completeness at flux limit $m_r < 19.8$ in equatorial fields, Liske et al. 2015). The full overlap between GAMA equatorial and KiDS and the unbiased selection of flux-limited spectroscopy in the former dataset allowed us to obtain very precise and accurate photometric redshift estimates for our lens sample, with mean bias $\langle \delta z \rangle = \langle z_{\text{phot}} - z_{\text{spec}} \rangle \simeq 10^{-4}$ and scatter $\sigma_{\delta z} \simeq 0.02(1+z)$. Thanks to the addition of VIKING data over the full KiDS-1000 area (Kuijken et al. 2019), the default photo- z solution is now based on 9-band photometry. In this work, however, we use redshifts obtained from the optical $ugri$ band photometry alone as, since the lens sample is bright and relatively low-redshift, NIR photometry does not significantly improve the photometric redshift estimation (see Bilicki et al. 2018 for more details). In

¹ <http://kids.strw.leidenuniv.nl>

addition, using the NIR photometry would introduce additional masking to our data, due to some gaps in VIKING coverage, which would reduce our lens galaxy sample. As we will show in Sect. 3, improving the redshift accuracy further (e.g. with NIR data) does not significantly increase the purity of our central sample, whereas increasing the survey area equips us with a larger sample for a more precise measurement. We restrict the lens redshifts to $0.1 < z_l < 0.5$, as outside of this range the photo- z s are less well constrained (Bilicki et al. 2018); this cut anyway removes a small fraction of the lens sample (< 10%).

Galaxy shapes for our source galaxy sample are measured using the THELI²-reduced r -band images with the *lensfit* shape measurement method (Miller et al. 2007, 2013, Giblin et al., in prep.). This method is a likelihood-based algorithm that fits surface brightness profiles to observed galaxy images, and takes into account the convolution with the PSF. Using a self-calibrating scheme, it has been shown to measure shear of galaxies to percent level accuracy, in simulated KiDS r -band images (Fenech Conti et al. 2017; Kannawadi et al. 2019).

Shears are obtained using *lensfit* for galaxies with an r -band magnitude larger than 20, which does not allow us to use these for shapes of our lens sample. In addition, *lensfit* is optimised for small SNR galaxies and a set-up for measuring bright galaxies is not readily available. To acquire shape information for our lens sample we apply the DEIMOS shape measurement method (Melchior et al. 2011) on the AstroWISE³ reduced r -band KiDS images.

DEIMOS is based on measuring weighted surface brightness moments from galaxy images and using these to infer the galaxy's ellipticity. Unlike other moment-based techniques, it allows for a mathematically accurate correction of the PSF convolution with the galaxy's light profile avoiding any assumptions on the profile or behaviour of the PSF. The accuracy of this correction is only limited by the accuracy of the PSF modelling. Moreover, a correction for the necessary radial weighting, employed during moment measurement, is used; higher-order moments are calculated in order to approximate the unweighted galaxy moments from measured weighted moments.

To model the PSF we use shapelets (Refregier 2003); orthogonal Hermite polynomials multiplied with Gaussian functions that can be linearly combined to describe image shapes. The process is described in Kuijken et al. (2015), where the model has been shown to perform very well in KiDS imaging data, displaying very small residual correlation between the modelled ellipticities and the ones measured by using the stars in the image. To measure galaxy moments, we use an elliptical Gaussian weight function, following a per-galaxy matching procedure. The size of the weight function is tied to the scale of this Gaussian, and we use two different scales in this work, equal to the isophote of the galaxies r_{iso} and $1.5r_{\text{iso}}$ (defined at 3σ above the background, see Georgiou et al. 2019b for more details). We use these two values to probe potential differences in the measured ellipticity ratio with the galaxy scale probed; a larger weight function will reveal more of the shape of the outer galaxy regions. Neighbouring sources in the image are masked using segmentation maps from SExtractor (Bertin & Arnouts 1996). A detailed description of the shape measurement process can be found in Georgiou et al. (2019b).

For the GAMA galaxy sample, which is very similar in properties to the lens sample used here, Georgiou et al. (2019b) showed that the multiplicative bias on the ellipticity (not shear) is

lower than 1%, and does not depend strongly on the galaxy properties. This is attributed to the great flexibility of the DEIMOS method, as well as the fact that these galaxies have a very high SNR in the KiDS imaging data (with a mean SNR ~ 300 in r -band images) and are generally very well resolved compared to the PSF size.

In our analysis, we do not probe the lensing signal on very large scales and, therefore, we do not subtract the signal around random points, which in any case has been shown to be consistent with zero in other KiDS weak lensing measurements (Dvornik et al. 2017). Additive bias in the shape measurements is not expected to bias the spherically averaged gravitational shear measurements. The anisotropic lensing measurements are not expected to be affected either, since sources and lenses were measured using different shape measurement methods, and any additive biases (which are anyway measured to be negligibly small) are not expected to be correlated. Multiplicative biases are also not expected to play a significant role, since they affect the isotropic and anisotropic lensing signal in the same way, which would leave the measurement of halo ellipticity unaffected. Furthermore, multiplicative bias for the lens shapes have been shown to be on the sub-percent level (Georgiou et al. 2019b), and do not affect the calculation of the position angle of the lens.

2.2. GAMA

GAMA⁴ (Driver et al. 2009, 2011; Liske et al. 2015) is a spectroscopic survey carried out with the Anglo-Australian Telescope, using the AAOmega multi-object spectrograph. It provides spectroscopic information for $\sim 300,000$ galaxies over five sky patches of $\sim 60 \text{ deg}^2$ area each for a total coverage of $\sim 286 \text{ deg}^2$. The three equatorial patches (G09, G12, G15) have a completeness of 98.5% and are flux limited to $r_{\text{petrosian}} < 19.8$ mag; out of the two south patches, G23 overlaps with the KiDS footprint and has a completeness of 94.5% with a flux limit $i < 19.2$ mag. This latter selection gives slightly lower mean redshift than in the equatorial fields, therefore for the lens photo- z training we used only the deeper and more complete equatorial data. We have verified that adding G23 does not improve the photo- z estimates (see Bilicki et al. 2021, for more details).

The unique aspect of the GAMA sample is the high completeness, together with the fact that no pre-selection is made on the target galaxies besides imposing a flux limit and removing stars and point-like quasars (Baldry et al. 2010). This nullifies any selection effects and provides the means to produce a highly pure and accurate group catalogue (Robotham et al. 2011). This catalogue is produced using a friends-of-friends based algorithm to define galaxy groups and assign galaxies to them. We use this group catalogue to validate our central galaxy sample selection from our lens galaxy sample, and quantify its purity, assuming the satellites identified in the catalogue to be the true satellites of the sample. We use the 10th version of this group catalogue, which does not contain the G23 region. After masking the lens sample according to the KiDS mask, we are left with $\sim 120,000$ galaxies matched with the group galaxy catalogue. In Fig. 1, we show the satellite fraction of the sample in bins of redshift; at higher redshift, satellites fall below the detection limit and the satellite fraction of the sample is decreases.

² <https://www.astro.uni-bonn.de/theli/>

³ <http://www.astro-wise.org/>

⁴ <http://www.gama-survey.org/>

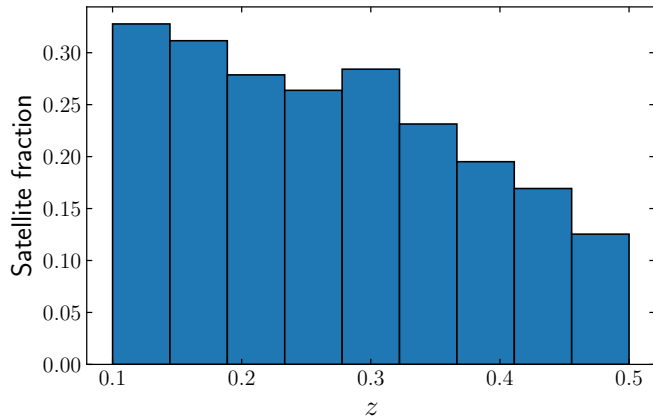


Fig. 1. The satellite fraction ($N_{\text{sat}}/N_{\text{all}}$) in the GAMA galaxy sample, in bins of redshift.

2.3. MICE

The GAMA group catalogue used in this work is susceptible to imperfections, especially for the more massive groups. Robotham et al. (2011) showed that the number of high richness groups was lower than what was expected from mock group catalogues specifically designed for validation of the group finding algorithm. In addition, Jakobs et al. (2018) found, using hydrodynamical simulations, that the group algorithm tends to fragment larger groups into smaller ones. Because of this, we choose to also validate our central sample selection using mock galaxy catalogues from a cosmological simulation, the MICE Grand Challenge run (Crocce et al. 2015).

MICE is an N-body simulation containing $\sim 70 \times 10^{10}$ dark-matter particles in a $(3h^{-1}\text{Gpc})^3$ comoving volume, from which a mock galaxy catalogue has been built, using Halo Occupation Distribution and Abundance Matching techniques (Carretero et al. 2015). Halos are resolved down to few $10^{11} M_{\odot}/h$. The catalogue contains information for a large number of galaxy properties, such as apparent magnitude, stellar mass, as well as a distinction of the galaxies into centrals and satellites, which we use in this work. Other applications of the catalogue include galaxy clustering, weak lensing and higher-order statistics (Fosalba et al. 2015a,b; Hoffmann et al. 2015). We downloaded the publicly available version 2 of the catalogue from cosmohub⁵ (Carretero et al. 2017). From the 5000 deg^2 that the whole mock catalogue covers, we cut out 200 deg^2 and select galaxies with apparent SDSS-like r -band magnitude of < 20.3 mag, to match the cut performed in Bilicki et al. (2018).

3. Central galaxy sample

3.1. The algorithm

In order to optimally extract the anisotropic weak lensing signal of elliptical dark matter halos, it is important to exclude galaxies in our sample that reside in sub-halos, i.e. satellite galaxies (see e.g. van Uitert et al. 2017). Because of the hierarchical structure formation, central galaxies are commonly found in overdense regions of the Universe where other neighbouring galaxies are also likely to be found. Based on this, we developed an algorithm to search for galaxies in our sample that have a high chance of being a central halo galaxy.

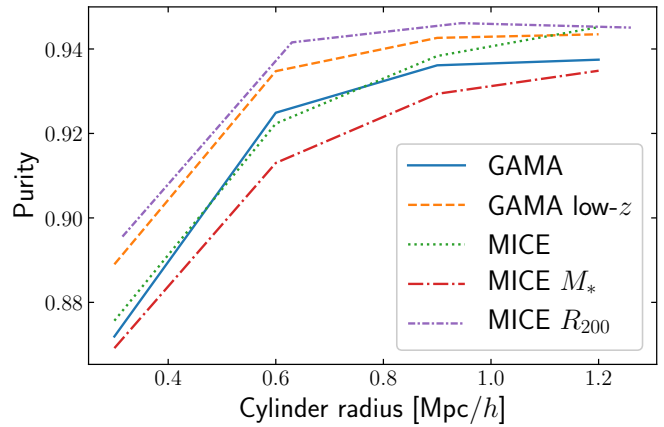


Fig. 2. Purity of our central galaxy sample, as a function of fixed cylinder radius used to identify centrals in overdense regions. Lines connect the individual points. In solid blue we show results from the GAMA+KiDS-1000 overlap, over the photometric redshift space of $0.1 < z < 0.5$. We also show the results for redshifts between $0.1 < z < 0.3$ with a dashed orange line. The dotted green line shows the purity of the sample obtained using the MICE2 mock catalogues, for $0.1 < z < 0.5$. The red dash-dotted line are results obtained when we look for the most massive (in terms of stellar mass) galaxy in the cylinder centre, instead of the brightest one. Finally, the purple dense dash-dotted line represents results obtained when, instead of a fixed cylinder radius we use multiples k of the galaxy's R_{200} to define the radius size, with $k = \{1, 2, 3, 4\}$. In this case, we plot the median value of the cylinder radius on the x -axis, corresponding to the four different values of purity obtained.

The algorithm is as follows: For every galaxy in our sample, we search for neighbouring galaxies inside a cylinder in sky and redshift space. The cylinder radius has a fixed physical length while the depth of the cylinder is determined by the accuracy of our redshift estimation. If neighbouring galaxies are indeed found, we ask the question whether the galaxy we selected, that lies in the middle of the cylinder, is the brightest galaxy (in the r -band) inside that cylinder. If this is true, we identify this galaxy as a central. We tested two different cylinder depths, $\pm dz$ and $\pm 2dz$ (where dz is the redshift uncertainty, equal to $\sim 0.02(1+z)$ for our lens galaxy sample) and chose the latter which was found to perform better.

3.2. Sample purity

We test the performance of this algorithm on the GAMA galaxy survey sample as well as the mock galaxy catalogues from the MICE simulation. The spectroscopic information together with the high completeness of the GAMA sample allows the construction of a highly accurate group galaxy catalogue, which we use here to identify central and satellite galaxies. We select central galaxies by removing any galaxy that is a satellite (we keep both brightest group galaxies as well as field galaxies, the latter are expected to live in their own isolated dark matter halo or have satellites around them too faint to detect).

However, imperfections are present in this group catalogue (see Sect. 2.3). Therefore, we also use the MICE mock galaxy catalogues to validate our algorithm, where we know a priori the central and satellite galaxies. We mimic the photometric redshift uncertainty in the mock catalogue redshifts by adding a random number to them, drawn from a Gaussian distribution with scale equal to the redshift uncertainty, i.e. $\sim 0.02(1+z)$.

⁵ <https://cosmohub.pic.es>

We show the performance of our algorithm in Fig. 2, where we plot the purity (number of true centrals we identify over the total number of centrals we identify) of our central galaxy sample, as a function of the fixed cylinder radius used. When using the GAMA survey as a reference, we see that we can achieve purity of up to $\sim 94\%$ for the largest cylinder radius. We can also see that the purity of the sample increases when a larger cylinder is used, which is expected as it is less likely to mis-identify a very bright nearby satellite as a central when using a larger cylinder, that is more likely to also contain the central galaxy.

We also check the purity of our sample in low-redshift galaxies ($0.1 < z < 0.3$) of the GAMA sample, where the satellite fraction remains high, around $\sim 27\%$ (Fig. 1), since the algorithm could under-perform in this satellite-rich redshift space. We find, however, that the purity of the central sample is higher in this regime, building confidence in the validity of our central sample selection.

Results from applying the algorithm to the MICE2 mock galaxy catalogue are also shown in Fig. 2. We see that the values for purity that we achieve are very similar to the values we get using GAMA, except for when using the largest cylinder radius. This means that, for the largest radius, the actual purity of our central sample is higher than the one we measure using GAMA.

In addition, we try to optimise our central selection by using the stellar masses in the mock galaxy catalogues. First, we modify the algorithm so as to select the most massive galaxy in the cylinder's centre, instead of the brightest one. For this, we use the stellar mass present in the MICE catalogues, and plot the purity in Fig. 2. The performance is worse compared to using apparent brightness, suggesting that the central galaxy is more often the brightest one in the halo, but not the most massive, in terms of stellar mass.

Lastly, instead of using a fixed cylinder radius to search for overdense regions, we use a per-galaxy cylinder radius, tied to the R_{200} of the galaxy. To compute this, we use the stellar-to-halo mass relation computed for GAMA central galaxies (van Uitert et al. 2016),

$$M_*^c(M_h) = M_{*,0} \frac{(M_h/M_{h,1})^{\beta_1}}{[1 + (M_h/M_{h,1})]^{\beta_1 - \beta_2}}, \quad (1)$$

where M_*^c is the stellar mass of the central galaxy and M_h the halo mass. We use the best-fit values from van Uitert et al. (2016) for the rest of the parameters in this model and solve numerically for M_h . We then compute the R_{200} from $M_h \equiv 4\pi(200\bar{\rho}_m)R_{200}^3/3$, where $\bar{\rho}_m = 8.74 \times 10^{10} h^2 M_\odot/\text{Mpc}^3$ is the comoving matter density. As can be seen from Fig. 2, the purity of the sample generally increases when using a more per-galaxy optimised cylinder.

It is clear that increasing the cylinder radius increases the purity of our central galaxy sample, but this comes at a cost. Specifically, the completeness of the sample drops as the radius increases, and we end up with fewer galaxies for our analysis. This is expected, as larger cylinders will encompass more and more central galaxies, making the sample less complete. Even the gain using the galaxy R_{200} as a cylinder radius causes the completeness to drop by $\sim 3\%$. It is, therefore, important to find a good compromise between the sample's purity and the total number of central galaxies that will be used.

As a last step in this direction, we look at the second brightest galaxy in the cylinder, and the difference in magnitude from the brightest one. If two galaxies are in the same overdensity but are too close in magnitude, it is possible that the centre of the halo does not correspond to the brightest galaxy. Therefore, we reject centrals that have a galaxy inside the same cylinder up to

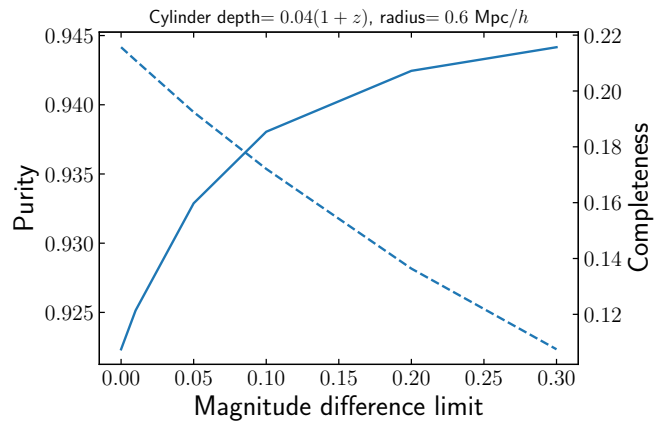


Fig. 3. Purity (solid, left y -axis) and completeness (dashed, right y -axis) of our central galaxy sample after rejecting centrals with a galaxy brighter than a magnitude difference from the central's brightness, shown on the x -axis. The cylinder used was fixed at $0.6 \text{ Mpc}/h$. Lines connect the individual points.

a magnitude difference limit. We plot the purity of the central sample following this procedure, as a function of the magnitude difference limit for a fixed cylinder of $0.6 \text{ Mpc}/h$ radius in Fig. 3. We see that the purity increases as the magnitude difference limit increases, but the completeness drops.

Based on this, we choose to use a magnitude difference limit of 0.1 in our final sample. To increase the sample size while not compromising much on its purity, we opt for using a fixed cylinder radius of $0.6 \text{ Mpc}/h$. With this setup, we achieve a purity of 93.4% , as quantified from the overlap with the GAMA group catalogue. The total number of central galaxies for the whole KiDS-1000 area, after masking, is 138,607. Shape measurements are successfully obtained for 115,930 galaxies using a weight function with scale equal to r_{iso} and 117,601 galaxies using $1.5r_{\text{iso}}$.

3.3. Scaling with photo- z accuracy

Interestingly, the purity of the sample seems to plateau for large cylinders. To understand this better, we repeated the analysis using the mock galaxy catalogues and sampling photometric redshifts with three different values of accuracy, $dz = \{0.02, 0.01, 0.0035\}(1+z)$. The first choice represents our lens galaxy sample, the second corresponds to the photometric redshifts achievable for Luminous Red Galaxies (LRGs, Rozo et al. 2016; Vakili et al. 2019), and the last one is the expected redshift accuracy from a narrow-band based survey, such as the Physics of the Accelerated Universe (PAUS Eriksen et al. 2019).

The results are shown in Fig. 4, where we plot the purity and completeness for the different redshift accuracies. We also change the size of the cylinder in redshift space according to the redshift accuracy. Interestingly, the purity of the sample remains roughly the same in all three cases. As the redshift accuracy and cylinder depth reduces, we see that the completeness of the sample increases as well. From this we conclude that improvements to the purity cannot be made by reducing the redshift uncertainty.

The lack of improvement in purity can be understood if in lower mass groups the central halo galaxy does not always correspond to the brightest galaxy (see e.g. Lange et al. 2018). Increasing the redshift accuracy allows for better determination of centrals in less massive halos, which, however, are expected to

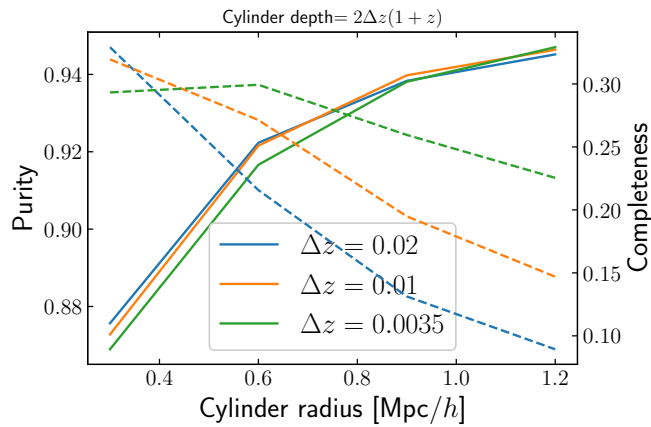


Fig. 4. Purity (solid lines) of our central galaxy sample selection as a function of the fixed cylinder radius. Lines connect the individual points. Results shown for three different simulated photometric redshift accuracies. The depth of the cylinder is equal to ± 2 times the redshift uncertainty. The completeness of the central galaxy sample is also shown, on the right y -axis, overplotted with dashed lines.

carry a weaker signal of halo ellipticity. Therefore, it is better to increase the area of the survey, if possible, instead of the redshift accuracy. This justifies our choice to use the much larger area KiDS-1000 data, compared to the spectroscopic redshifts of the GAMA survey, for our analysis.

3.4. Sample characteristics

We present here the characteristics of the final sample of central galaxies we compiled. The sample's properties are obtained for the overlap of our KiDS-1000 sample with the GAMA survey, where an extensive photometry and stellar mass catalogue is used (StellarMassesLambdarv20, Taylor et al. 2011; Wright et al. 2016). This catalogue provides estimates of the stellar mass, absolute magnitudes and restframe colours of galaxies using fits to galaxy SEDs from photometry in the optical+NIR broad bands.

In addition, we split the central sample into intrinsically red and blue galaxies. To do so, we isolate the red sequence galaxies by inspecting the distribution of apparent $g - i$ colour versus m_r in 10 linear redshift bins in the redshift range of the lens sample. With this division, we obtain 62426 red and 53504 blue lens galaxy sub-samples. Their average ellipticity modulo is the same as for the full sample, but their distributions show that slightly more blue galaxies have ellipticities with absolute values below 0.1 or above 0.3 than red galaxies do.

In the top panel of Fig. 5 we show the distribution of stellar mass for the full galaxy population in the bright KiDS-1000 sample (restricted to the overlap with GAMA), as well as for our central galaxy sample, divided also into red and blue centrals. The central galaxies are generally more massive than galaxies in the whole population, as we would expect. The mean stellar mass of the red and blue central sample is $\sim 10^{11} M_\odot$ and $10^{10.6} M_\odot$, respectively.

In addition to this, we show the distribution of restframe $g - i$ colours, corrected for dust extinction, in the bottom panel of Fig. 5, again for the full KiDS-1000 and central (all, blue and red) galaxy sample. We see that the central galaxy sample consists of generally more red galaxies than the full sample. We also see that the colour distributions of our selection of red and blue cen-

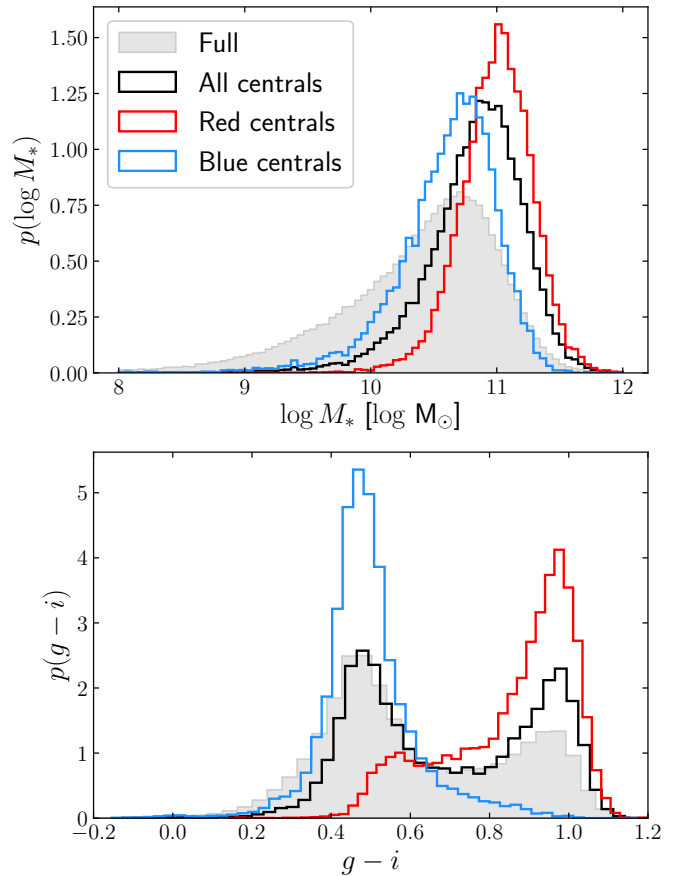


Fig. 5. Top: normalised distribution of stellar mass of the full sample (in filled grey) and our central galaxy sample (in black, red and blue for all, red and blue centrals, respectively) in the GAMA overlap. Bottom: normalised distribution of restframe, dust corrected $g - i$ colour for the same galaxy samples.

trals generally follows the expected restframe $g - i$ distribution, building confidence in our colour selection. We note, that a small number of relatively blue galaxies enter our red galaxy sample, which is an effect of our imperfect colour split based on photometric redshift data and a visual inspection. However, given the number of these galaxies, we do not expect a cleaner sample selection to alter our results.

4. Methodology

Gravitational lensing has the effect of coherently distorting light rays of background galaxies (sources) from the intervening matter along the line of sight. Since galaxies are biased tracers of the matter density in the Universe, one expects to find a correlation between the position of foreground galaxies (lenses) and source galaxy shapes. In its weak regime, the effect is very small, and the observed ellipticities of source galaxies are only affected on the order of 1%. Large statistical ensembles of lens-source galaxy pairs are therefore required to extract the weak lensing signal.

In this work, both for lens and source galaxies, we use the third flattening, $\epsilon = \epsilon_1 + i\epsilon_2$, as an ellipticity measure, which is related to the semi-minor to semi-major axis ratio, q , by $|\epsilon| = (1 - q)/(1 + q)$. We can then express the tangential and cross

ellipticity of source galaxies with respect to the lens position as

$$\epsilon_+ = -\epsilon_1 \cos(2\theta) - \epsilon_2 \sin(2\theta), \quad (2)$$

$$\epsilon_\times = \epsilon_1 \sin(2\theta) - \epsilon_2 \cos(2\theta), \quad (3)$$

where θ is the position angle of the line connecting the lens-source galaxy pair. When averaged over pairs, ϵ_+ provides an unbiased but noisy estimate of the gravitational shear γ , i.e. $\langle \epsilon_+ \rangle \approx \gamma_+$, which can then be related to the excess surface mass density through

$$\Delta\Sigma(R) = \bar{\Sigma}(< R) - \Sigma(R) = \gamma_+(R)\Sigma_{\text{crit}}, \quad (4)$$

with Σ_{crit} the critical surface density, defined by

$$\Sigma_{\text{crit}} = \frac{c^2}{4\pi G} \frac{D_s}{D_l D_{ls}}. \quad (5)$$

In the above equation, c and G are the speed of light and gravitational constant, respectively, D_s is the angular diameter distance to the source galaxy, D_l to the lens galaxy and D_{ls} between the lens and source galaxy. Note that (4) holds true only when considering an azimuthally averaged ensemble of lenses.

The isotropic (azimuthally averaged) part of the lensing signal can be calculated from the data using the estimator

$$\widehat{\Delta\Sigma} = \left(\frac{\sum_{ls} w_{ls} \epsilon_+ \Sigma_{\text{crit}}}{\sum_{ls} w_{ls}} \right), \quad (6)$$

where the sum runs over all lens-source galaxy pairs, that fall in a given projected radius bin. We weight each pair with ellipticity weights, w_s , computed by *lensfit*, which accounts for uncertainty in the shear estimate, and define

$$w_{ls} = w_s \Sigma_{\text{crit}}^{-2}. \quad (7)$$

Since galaxy redshifts are computed through photometry, it is important to account for the full posterior redshift distribution of source galaxies, $p(z_s)$ (see Sect. 2.1), when computing Σ_{crit} . This is done with equation

$$\Sigma_{\text{crit}}^{-1} = \frac{4\pi G}{c^2} \int_{z_l}^{\infty} \frac{D_l(z_l) D_{ls}(z_l, z_s)}{D_s(z_s)} p(z_s) dz_s. \quad (8)$$

4.1. Anisotropic lensing model

We model the anisotropic part of the lensing signal following the formalism presented in Schrabback et al. (2015) which is based on work by Natarajan & Refregier (2000) and Mandelbaum et al. (2006). The excess surface mass density of a lens is modelled as

$$\Delta\Sigma_{\text{model}}(r, \Delta\theta) = \Delta\Sigma_{\text{iso}}(r) [1 + 4f_{\text{rel}}(r)|\epsilon_{h,a}| \cos(2\Delta\theta)]. \quad (9)$$

In the above, $\Delta\Sigma_{\text{iso}}$ is the excess surface mass density for a spherical halo (estimated from data using Eq. (6)) and $\Delta\theta$ is the position angle coordinate in the lens plane, measured from the halo's semi-major axis. The ellipticity of the halo is probed by the galaxy's ellipticity, therefore, we are sensitive only to the aligned component of the halo ellipticity with the galaxy, $|\epsilon_{h,a}|$. The anisotropy of the elliptical halo's lensing is described by $f_{\text{rel}}(r)$, which depends on the assumed halo density profile and is generally a function of the projected separation r . For elliptical halos not described by a single power-law, $f_{\text{rel}}(r)$ needs to be computed numerically (see e.g. Mandelbaum et al. 2006), and we interpolate this quantity (using a cubic interpolation) from tabulated values. In order to avoid systematic biases in our

anisotropic lensing signal measurement, it is also necessary to define the excess surface mass with lens and source ellipticities rotated by $\pi/4$, where we have

$$\Delta\Sigma_{45, \text{model}}(r, \Delta\theta) = \Delta\Sigma_{\text{iso}}(r) [4f_{\text{rel}, 45}(r)|\epsilon_{h,a}| \cos(2\Delta\theta + \pi/2)], \quad (10)$$

where $f_{\text{rel}, 45}(r)$ is obtained in the same manner as $f_{\text{rel}}(r)$.

The quantity of interest is the ratio of the halo ellipticity modulo to the galaxy ellipticity modulo, $\tilde{f}_h = |\epsilon_h|/|\epsilon_g|$. However, we can only measure this quantity weighted by the average mis-alignment angle between the halo and host galaxy's semi-major axis, $\Delta\phi_{h,g}$. Consequently, the measured quantity $f_h = \tilde{f}_h \langle \cos(2\Delta\phi_{h,g}) \rangle$ (where we also assume that the mis-alignment angle does not depend on $|\epsilon_h|$). In order to extract f_h from data, we use the following estimators,

$$\widehat{f\Delta\Sigma} = \frac{\sum_{ls} w_{ls} \epsilon_+ \Sigma_{\text{crit}} |\epsilon_l| \cos(2\phi_{ls})}{\sum_{ls} w_{ls} |\epsilon_l|^2 \cos^2(2\phi_{ls})}, \quad (11)$$

and

$$\widehat{f_{45}\Delta\Sigma} = -\frac{\sum_{ls} w_{ls} \epsilon_\times \Sigma_{\text{crit}} |\epsilon_l| \sin(2\phi_{ls})}{\sum_{ls} w_{ls} |\epsilon_l|^2 \sin^2(2\phi_{ls})}, \quad (12)$$

where ϕ_{ls} is the angle between the lens semi-major axis and the position vector connecting the lens-source galaxy pair. These two estimators can be predicted from $f_h f_{\text{rel}} \Delta\Sigma_{\text{iso}}$ and $f_h f_{\text{rel}, 45} \Delta\Sigma_{\text{iso}}$, respectively. However, the estimators are easily contaminated by systematic errors in the lensing signal measurements, such as imperfections due to incorrect PSF modelling or cosmic shear from structures between the lens and the observer (Mandelbaum et al. 2006; Schrabback et al. 2015). An estimator insensitive to these systematic effects can be constructed by subtracting the two,

$$\widehat{(f - f_{45})\Delta\Sigma} = \widehat{f\Delta\Sigma} - \widehat{f_{45}\Delta\Sigma}. \quad (13)$$

For measuring the ellipticity ratio, we use this estimator, and the analysis we follow is described below.

4.2. Extracting f_h

To measure f_h from data, we consider the two estimators $x_i = \widehat{\Delta\Sigma}_i$ and $y_i = (\widehat{f} - \widehat{f_{45}})\Delta\Sigma_i / (f_{\text{rel}}(r_i) - f_{\text{ref}, 45}(r_i))$, where the index i runs over the radial bins over which we calculate the lensing signal and r_i is the central value of that bin. These are two random Gaussian variables, which prohibits us from simply computing their fraction $m = y_i/x_i$, which would lead to a biased estimate of f_h . To overcome this, we consider, for a given m , the quantity $y_i - mx_i$. This is a random Gaussian variable drawn from $N(0, w_i^{-1})$, with $w_i^{-1} = \sigma_y^2 + m^2 \sigma_x^2$ and σ_x, σ_y are the error on the measured estimators x_i and y_i , respectively (Mandelbaum et al. 2006).

The following sum ratio

$$\frac{\sum_i w_i (y_i - mx_i)}{\sum_i w_i} \sim N\left(0, \frac{1}{\sum_i w_i}\right) \quad (14)$$

is also a random Gaussian variable. Based on this, we determine confidence intervals of $\pm 1\sigma$ in measuring m , by considering the inequality

$$\frac{-Z}{\sqrt{\sum_i w_i}} < \frac{\sum_i w_i (y_i - mx_i)}{\sum_i w_i} < \frac{+Z}{\sqrt{\sum_i w_i}}. \quad (15)$$

We use m drawn from a grid and calculate f_h by requiring $f_h = m(Z = 0)$. We also determine the $\pm 1\sigma$ intervals by setting $Z =$

± 1 . In addition, we compute the reduced χ^2 from n radial bins using

$$\chi^2_{\text{red}} = \frac{\sum_i w_i (y_i - m(Z=0)x_i)^2}{n-1}. \quad (16)$$

This method does not take into account the off-diagonal elements of the covariance matrix of our measurements. These, however, were estimated to be very small (see Sect. 5), with the standard deviation of the correlation matrix off-diagonal elements being 4×10^{-2} .

5. Halo Ellipticity

We measure the weak lensing signal around our central galaxy sample using 25 radial bins, logarithmically spaced between 20 kpc/h and 1.2 Mpc/h. We restrict the sample to lens galaxies with well defined ellipticities, $0.05 < \epsilon_l < 0.95$. The median redshift of the lenses is 0.26 and their average ellipticity is 0.188 for shapes obtained using weight function of r_{iso} and 0.183 when using $1.5r_{\text{iso}}$. We fit the isotropic weak lensing signal with an NFW profile (Navarro et al. 1996; Wright & Brainerd 2000), while fixing the concentration-mass relation to Duffy et al. (2008),

$$c = 5.71 \left(\frac{M_{200}}{2 \times 10^{12} M_{\odot}/h} \right)^{-0.084} (1+z)^{-0.47}, \quad (17)$$

to finally obtaining an estimate for the scale radius r_s . This is then used to calculate $f_{\text{rel}}(r)$ and $f_{\text{rel},45}(r)$. We note that our measurements of f_h are not very sensitive to the concentration-mass relation. Changing the constant in Eq. (17) by 20% shifts our measured value by at most $\sim 0.3\sigma$, therefore we do not consider a more complicated relation. In NFW profile fits, we use the mean redshift of the full lens sample. We also restrict the fit to the range from 40 kpc/h up to 200 kpc/h. The first limit minimises signal from baryons in the centre of the halo, as well as contamination of the source galaxy's shear by the extended light of each lens (Schrabback et al. 2015; Sifón et al. 2018). The upper limit ensures that we do not include contributions from the 2-halo term when fitting the lensing signal. This is a conservative limit since we do not expect a strong 2-halo term in our lensing signal given that our galaxy sample has very small satellite galaxy contamination.

To calculate the covariance of our measurements we use a bootstrap technique. We sample 10^5 random bootstrap samples from the lens catalogue (with replacement) and use this data vector to calculate the covariance matrix, obtaining error bars for our measurements from its diagonal elements. This technique ignores errors due to sample variance from large-scale structure. However, these are expected to be negligible given the scales we probe. We test this by computing the covariance and errors from a per-area bootstrap technique, dividing the survey into 1 deg² patches and computing the lensing signal in each patch. We then select 10^5 random bootstrap patches, weighting them by the number of lenses (since patches with significantly fewer than average lenses will have a more uncertain signal measurement) and arrive at fully consistent error bars. We also find the off-diagonal elements of the covariance matrix to be negligible on all scales, justifying the analysis outlined in Sect. 4.2.

We present our measurements in Fig. 6 for the case when the shape of the lens galaxy is measured using a weight function with scale equal to r_{iso} . Results around the full, red and blue lens galaxy sample are shown in the left, right and middle column, respectively. The first row shows the isotropic lensing

signal measurement, spherically averaged, as well as the best-fit NFW profile, with the ranges used in the fit indicated with dashed vertical lines. We also overplot the isotropic lensing signal obtained from the full KiDS-1000 bright-end catalogue in the same redshift range in the top left panel, for comparison. We see that our central galaxy sample is generally more massive and is not affected by a strong 2-halo term, contrary to the full sample. The resulting average halo mass for the three sub-samples can be seen in Table 1. We have also checked that $\Delta\Sigma_{45}$, which is calculated by substituting the tangential with the cross ellipticity component in Eq. (6), is consistent with zero across all measured scales. This is expected, since a spherically averaged cross component is not generated by gravitational lensing, and serves as a useful sanity check for a potential systematic offset.

In the next three rows of Fig. 6, we present the measurement of the anisotropic lensing signal for the three sub-samples. We use these measurements to calculate the ellipticity ratio, f_h , following Sect. 4.2, as well as the $1-\sigma$ confidence intervals. For the f_h measurement, we use scales from 40 kpc/h up to the estimated r_{200} for the corresponding galaxy sample, which can be seen as dashed lines in the figure. For visualisation, we overplot the best-fit NFW profile of the corresponding galaxy sample, multiplied by f_{rel} , $f_{\text{rel},45}$ or their difference, accordingly, as well as the best-fit value of f_h .

The resulting values of f_h , as well as the reduced χ^2 of the fit are presented in Table 1. We see that the ellipticity ratio is fitted reasonably well, as expressed by the χ^2 values. For the full sample we measure an ellipticity ratio of 0.27 with a 1.5σ statistical significance. For the red galaxies, the measured ratio is higher, 0.34, and the significance also increases to 2σ . Finally, we do not measure a significant ellipticity ratio for blue galaxies.

5.1. Mis-alignment dependence on galaxy scale

Following the results presented in the previous section, we re-measure the ellipticity ratio, f_h , using lens galaxy shapes with a weight function of scale equal to $1.5r_{\text{iso}}$. By using a larger weight function, the measured shapes will be more sensitive to the morphology of outer galaxy regions. The mean ellipticity of the lens sample is measured to be very similar when using the two weight functions (with a difference of 0.005) and their distributions were inspected to be nearly the same. Therefore, any difference measured in f_h will be directly related to differences in the mean mis-alignment angle, $\langle \cos(2\Delta\phi_{h,g}) \rangle$.

The isotropic lensing signal obtained with the larger weight function is statistically the same, given that the lensing sample is not systematically different. We show the anisotropic lensing measurements in the last row of Figure 6 with green diamonds, and the model obtained using the best-fit f_h for a large weight function with a dashed red line (see also Table 1). The measured signal for $(f - f_{45})\Delta\Sigma$ is higher, although only at a level of $\sim 1\sigma$. When analysing the full sample, we measure an $f_h = 0.50 \pm 0.20$, which is ~ 1.5 times higher than the value obtained using the smaller weight function. Looking at the red and blue galaxy sub-samples, we find $f_h = 0.55 \pm 0.19$ and $f_h = 0.28 \pm 0.55$, respectively, both of which are higher than the values obtained by using a smaller weight function. For red galaxies the detection of a non-zero ellipticity ratio is increased to 2.9σ , while blue galaxies are still found to have a value f_h fully consistent with zero.

From this analysis it is suggested that outer galaxy regions are more aligned with the shape of the dark matter halo. This is in agreement with other observations, where central galaxies were found to be more aligned with their satellite galaxy distributions

Table 1. Results from fits to the weak lensing signal, for the full sample, as well as the red and blue central galaxy sub-samples. The mean stellar mass is shown for galaxies in the KiDS-1000 and GAMA overlap, quoted from the StellarMassesLambdarv20 catalogue. We also show the best-fit and error of M_{200} from the NFW profile fits to the isotropic weak lensing signal as well as the resulting ellipticity ratio f_h fit, with its reduced χ^2 , according to Sect. 4.2, obtained using the two different weight function sizes to measure lens galaxy shapes (see Sect. 2.1).

Sample	$M_* [10^{10} M_\odot]$	$M_{200} [10^{12} M_\odot]$	$f_h (r_{\text{wf}}/r_{\text{iso}} = 1)$	$\chi^2_{\text{red}} (r_{\text{wf}}/r_{\text{iso}} = 1)$	$f_h (r_{\text{wf}}/r_{\text{iso}} = 1.5)$	$\chi^2_{\text{red}} (r_{\text{wf}}/r_{\text{iso}} = 1.5)$
Full	9.28	3.74 ± 0.16	$0.27^{+0.19}_{-0.18}$	1.14	0.50 ± 0.20	1.41
Red	12.14	6.69 ± 0.30	0.34 ± 0.17	0.80	0.55 ± 0.19	0.90
Blue	5.63	1.35 ± 0.14	$0.08^{+0.53}_{-0.53}$	0.83	0.28 ± 0.55	1.23

if the shape measurement used was more sensitive to their outer regions (Huang et al. 2016; Georgiou et al. 2019a). The physical processes causing this behaviour can be either tidal interactions between the central galaxy and the dark matter halo affecting the outer, less bound galaxy regions more strongly, or the fact that infalling material to the central galaxy generally follows the ellipticity of the dark matter halo.

5.2. Comparison with the literature

Our analysis closely follows work done in previous studies. Mandelbaum et al. (2006) used a very similar estimator on a much larger lens sample, split in colour and luminosity. For their L6 luminosity bin, which is closer to the mean luminosity of our sample, they found $f_h = 0.29 \pm 0.12$ for red and $f_h = 1.0^{+1.3}_{-0.9}$ for blue galaxies, but note that a sign inconsistency in their model computation might have affected these results (Schrabback et al. 2015). van Uitert et al. (2012) also studied a large lens sample consisting of less massive galaxies than ours, and found $f_h = 0.19 \pm 0.10$, 0.13 ± 0.15 and $-0.16^{+0.18}_{-0.19}$ for all, red and blue lens samples, respectively. Following the same methodology, Schrabback et al. (2015) studied a sample of lenses split in colour and stellar mass, and found $f_h = -0.04 \pm 0.25$ for all red lenses and $f_h = 0.69^{+0.37}_{-0.36}$ for all blue ones. They also provided predictions of f_h from the Millennium Simulation (Springel et al. 2005), which agrees with the values we obtain here. The studies above used almost identical methodology as in this work and lens samples much larger than ours, but which were likely contaminated by satellite galaxies. Our study indicates the importance of selecting central galaxies for an anisotropic lensing signal measurement.

The pioneering work of Hoekstra et al. (2004) and Parker et al. (2007), conducted similar measurements of f_h for single band photometric data and found $f_h = 0.77^{+0.18}_{-0.21}$ and $f_h = 0.76 \pm 0.10$, respectively. However, these results were not corrected for the spurious signal introduced by other effects that align lens and source ellipticities. This may have biased the resulting f_h measurements to high values (Schrabback et al. 2015).

Focussing on the brightest group galaxies (BGG) of the GAMA group catalogue specifically (using groups with more than 5 members), van Uitert et al. (2017) detected an halo ellipticity of $\epsilon_h = 0.38 \pm 0.12$, using the BGG semi-major axis as a proxy for the halo's orientation and focussing on scales below 250 kpc. Similar ellipticity has also been detected for dark matter halos of galaxy clusters (Evans & Bridle 2009; Clampitt & Jain 2016; Shin et al. 2018; Umetsu et al. 2018). For comparison, we find $\epsilon_h = 0.051^{+0.036}_{-0.034}$ for the full sample and $\epsilon_h = 0.064 \pm 0.032$ for red galaxies, using the average lens galaxy ellipticity of our sample and assuming zero mis-alignment angle.

Note that galaxies in these groups and clusters are generally more massive than our central galaxy sample (see Table

1), with the GAMA BGG sample having a mean stellar mass of $2.25 \times 10^{11} M_\odot$, and cluster central galaxies being typically more massive than that. In order to check whether more massive galaxies in our sample have an higher ellipticity ratio, we select galaxies based on stellar mass, obtained by running Le Phare (Ilbert et al. 2006) on the KiDS-1000 9-band photometry (Wright et al. in prep.). Using all galaxies with $M_* > 1.58 \times 10^{11} M_\odot$ we find $f_h = 0.24 \pm 0.19$, which is slightly higher than the value for the whole sample.

The ellipticity we obtain is significantly lower than what is measured in galaxy groups. This suggests that either halos of galaxy groups and clusters are more elliptical than those of relatively isolated galaxies⁶ or that the mean misalignment between halos and galaxies is smaller for group and cluster central galaxies. In cosmological simulations, higher mass halos where found to be more elliptical and less misaligned with their host galaxy than lower mass ones, which agrees with the trend observed here (e.g. Tenneti et al. 2014; Velliscig et al. 2015; Chisari et al. 2017). However, we do not measure a significant increase in f_h when we restrict our sample to high stellar mass galaxies, which leaves the interpretation unclear.

Another possible reason for the discrepancy may be differences in the shape measurement of the lenses. Shapes of lens galaxies were derived using a generally large weight function in van Uitert et al. (2017) (private communication). We measure a larger f_h when using a larger weight function for measuring shapes of lens galaxies in our sample, which might explain at least part of the low halo ellipticity value we find in comparison to galaxy groups.

6. Conclusions

In this work we measure the anisotropic lensing signal and halo-to-galaxy ellipticity ratio of galaxies for a bright sample ($m_r \lesssim 20$) with accurate redshifts acquired through a machine learning technique, trained on a similar spectroscopic sample (GAMA, $m_{r,\text{petro}} < 19.8$). We minimize satellite contamination, as it would complicate the interpretation and modelling of the measured signal. To construct the sample, we identify galaxies in regions of high galaxy number density and select the brightest one (in r -band) in a cylindrical area. We assess the purity of our central galaxy sample using the overlap with GAMA and find the purity to be = 93.4%. Similar values were obtained using the MICE mock galaxy catalogues (built from N-body cosmological simulations).

We use the central galaxy sample as lens galaxies and background sources from the KiDS-1000 shear catalogues. We also

⁶ Our sample consists of both BGG and field galaxies, the latter expected to be either isolated galaxies or BGGs of groups whose satellites are too faint to be detected within the imposed magnitude limit.

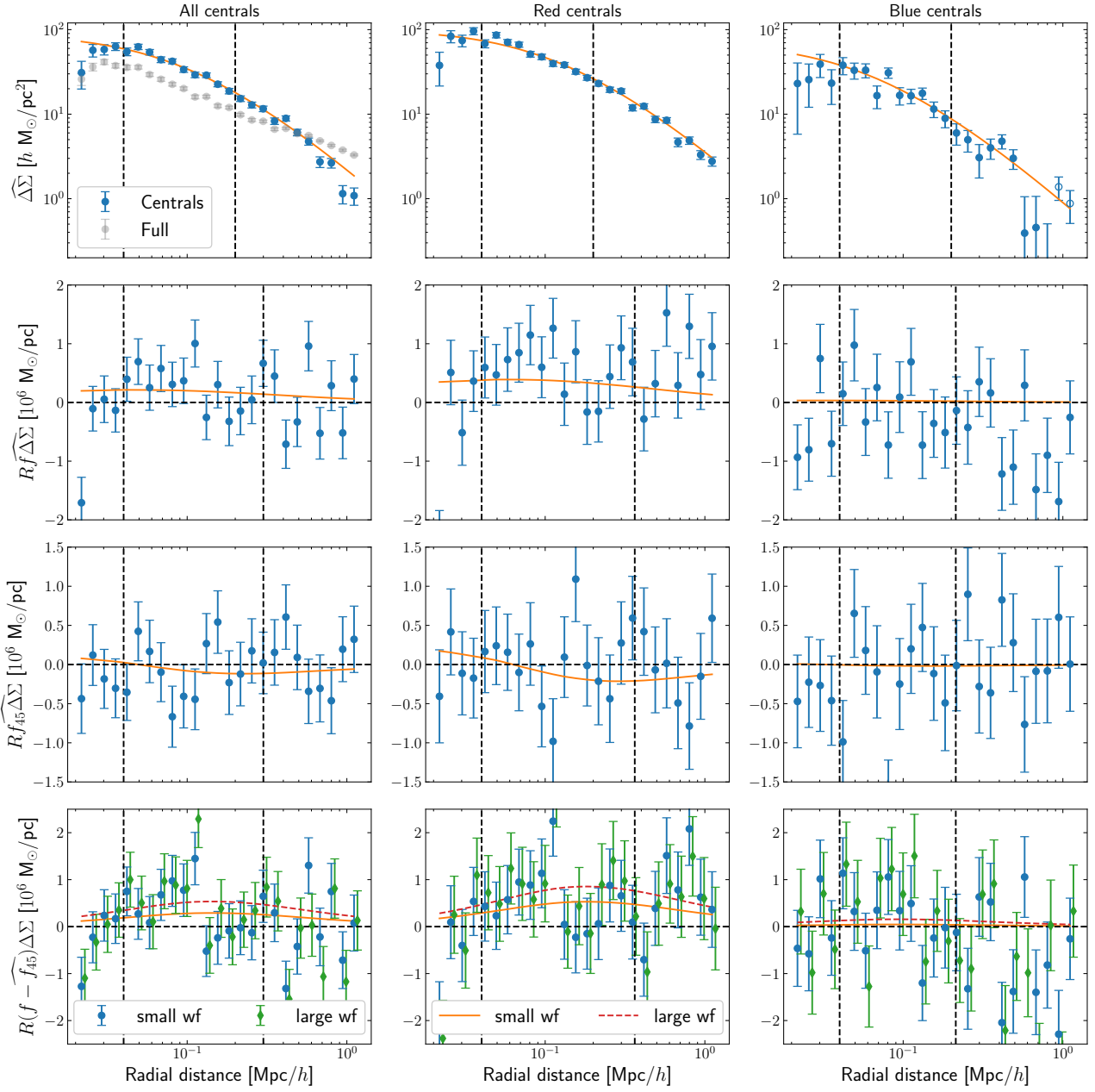


Fig. 6. Measurements of the weak lensing signal around our central galaxy sample. The first column shows results obtained for all centrals, while the second and third columns show results for the red and blue sub-samples, respectively (with open circles placed for negative measurements). The first row shows the isotropic lensing signal, the second and third row show the anisotropic lensing signal obtained with the estimators of Eqs. (11)–(12), while the last row shows the difference, Eq. (13). The best-fit NFW profile is overplotted on the first row, with dashed vertical lines depicting the ranges that were used during the fit. We also show the isotropic lensing signal of the full KiDS-1000 sample in grey points, as a comparison to the signal obtain using only the central galaxies. For the next rows we show the best-fit NFW profile multiplied by the best-fit f_h and f_{rel} , $f_{rel,45}$ and their difference, respectively, as well as the ranges used during the fit with dashed lines. In the last row, with green diamonds and red dashed line we show the data and model with the best-fit f_h obtained using a larger weight function of $r_{wf} = 1.5r_{iso}$ for measuring the lens galaxy shapes.

split the lens sample in intrinsically red and blue galaxies. Using the measured lensing signal, we extract the ellipticity ratio f_h (weighted by the misalignment angle between the galaxy and the halo semi-major axis) using an estimator unaffected by systematic errors, such as incorrect PSF modelling and cosmic shear. We measure $f_h = 0.27^{+0.19}_{-0.18}$ for the full sample and $f_h = 0.34 \pm 0.17$ for an intrinsically red sub-sample, respectively, while for blue galaxies the ratio is fully consistent with zero. Our measurements are in agreement with predictions based

on cosmological simulations and we demonstrate the importance of using a highly pure sample of central galaxies for the halo ellipticity measurement.

Our results are generally in agreement with studies of similar galaxy samples. However, we find a significantly lower halo ellipticity when we compare to central galaxies of galaxy groups and clusters. Cosmological simulations predict that lower mass halos are rounder and/or more misaligned with their host halo than more massive ones, which may explain part of this dif-

ference. Using shape estimates that are more sensitive to outer galaxy regions, we find a higher value for f_h , specifically 0.5 ± 0.2 and 0.55 ± 0.19 for the full and red sample, respectively, rejecting the hypothesis of round halos and/or randomly aligned galaxies with respect to their parent halo at 2.5 and 2.9σ . This suggests there is a galaxy-scale dependence of the mis-alignment angle $\Delta\phi_{hg}$, with outer regions of the host galaxy being more aligned with its dark matter halo.

Our results can also be connected with the difference found between the predicted galaxy intrinsic alignment signal of dark matter halos and the observationally measured alignment of galaxies, which are found to have a much lower signal (e.g. [Fallenbacher et al. 2009](#); [Okumura et al. 2009](#)). In addition, galaxy intrinsic alignments have been observed to depend on the galaxy properties, with more luminous (and therefore massive) galaxies indicating a stronger alignment amplitude than less luminous ones ([Singh et al. 2015](#); [Johnston et al. 2019](#)). This trend of the alignment signal is in the same direction with the decreasing misalignment of halos and galaxies with increasing halo mass seen here and in cosmological simulations.

References

Alam, S., Ata, M., Bailey, S., et al. 2017, MNRAS, 470, 2617

Anderson, L., Aubourg, É., Bailey, S., et al. 2014, MNRAS, 441, 24

Azzaro, M., Patiri, S. G., Prada, F., & Zentner, A. R. 2007, MNRAS, 376, L43

Bailin, J., Power, C., Norberg, P., Zaritsky, D., & Gibson, B. K. 2008, MNRAS, 390, 1133

Baldry, I. K., Robotham, A. S. G., Hill, D. T., et al. 2010, MNRAS, 404, 86

Banerjee, A. & Jog, C. J. 2008, ApJ, 685, 254

Bartelmann, M. & Schneider, P. 2001, Phys. Rep., 340, 291

Bautista, J. E., Vargas-Magaña, M., Dawson, K. S., et al. 2018, ApJ, 863, 110

Benítez, N. 2000, ApJ, 536, 571

Bertin, E. & Arnouts, S. 1996, A&AS, 117, 393

Bilicki, M., Dvornik, A., Hoekstra, H., et al. 2021, arXiv e-prints, arXiv:2101.06010

Bilicki, M., Hoekstra, H., Brown, M. J. I., et al. 2018, A&A, 616, A69

Brainerd, T. G. 2005, ApJ, 628, L101

Caminha, G. B., Grillo, C., Rosati, P., et al. 2016, A&A, 587, A80

Carretero, J., Castander, F. J., Gaztañaga, E., Crocce, M., & Fosalba, P. 2015, MNRAS, 447, 646

Carretero, J. et al. 2017, PoS, EPS-HEP2017, 488

Chisari, N. E., Koukoufilippas, N., Jindal, A., et al. 2017, MNRAS, 472, 1163

Clampitt, J. & Jain, B. 2016, MNRAS, 457, 4135

Coe, D., Benítez, N., Sánchez, S. F., et al. 2006, AJ, 132, 926

Corless, V. L., King, L. J., & Clowe, D. 2009, MNRAS, 393, 1235

Crocce, M., Castander, F. J., Gaztañaga, E., Fosalba, P., & Carretero, J. 2015, MNRAS, 453, 1513

de Jong, J. T. A., Verdoes Kleijn, G. A., Boxhoorn, D. R., et al. 2015, A&A, 582, A62

de Jong, J. T. A., Verdoes Kleijn, G. A., Erben, T., et al. 2017, A&A, 604, A134

Donahue, M., Ettori, S., Rasia, E., et al. 2016, ApJ, 819, 36

Driver, S. P., Hill, D. T., Kelvin, L. S., et al. 2011, MNRAS, 413, 971

Driver, S. P., Norberg, P., Baldry, I. K., et al. 2009, Astronomy and Geophysics, 50, 5.12

Dubinski, J. & Carlberg, R. G. 1991, ApJ, 378, 496

Duffy, A. R., Schaye, J., Kay, S. T., & Dalla Vecchia, C. 2008, MNRAS, 390, L64

Dvornik, A., Cacciato, M., Kuijken, K., et al. 2017, MNRAS, 468, 3251

Edge, A., Sutherland, W., Kuijken, K., et al. 2013, The Messenger, 154, 32

Elahi, P. J., Mahdi, H. S., Power, C., & Lewis, G. F. 2014, MNRAS, 444, 2333

Eriksen, M., Alarcon, A., Gaztanaga, E., et al. 2019, MNRAS, 484, 4200

Evans, A. K. D. & Bridle, S. 2009, ApJ, 695, 1446

Faltenbacher, A., Li, C., White, S. D. M., et al. 2009, Research in Astronomy and Astrophysics, 9, 41

Fenech Conti, I., Herbonnet, R., Hoekstra, H., et al. 2017, MNRAS, 467, 1627

Fosalba, P., Crocce, M., Gaztañaga, E., & Castander, F. J. 2015a, MNRAS, 448, 2987

Fosalba, P., Gaztañaga, E., Castander, F. J., & Crocce, M. 2015b, MNRAS, 447, 1319

Georgiou, C., Chisari, N. E., Fortuna, M. C., et al. 2019a, A&A, 628, A31

Georgiou, C., Johnston, H., Hoekstra, H., et al. 2019b, A&A, 622, A90

Hellwing, W. A., Cautun, M., Knebe, A., Juszkiewicz, R., & Knollmann, S. 2013, J. Cosmology Astropart. Phys., 2013, 012

Helmi, A. 2004, MNRAS, 351, 643

Hildebrandt, H., Köhlinger, F., van den Busch, J. L., et al. 2020, A&A, 633, A69

Hoekstra, H., Yee, H. K. C., & Gladders, M. D. 2004, in IAU Symposium, Vol. 220, Dark Matter in Galaxies, ed. S. Ryder, D. Pisano, M. Walker, & K. Freeman, 439

Hoffmann, K., Bel, J., Gaztañaga, E., et al. 2015, MNRAS, 447, 1724

Huang, H.-J., Mandelbaum, R., Freeman, P. E., et al. 2016, MNRAS, 463, 222

Hui, X., Ford, H. C., Freeman, K. C., & Dopita, M. A. 1995, ApJ, 449, 592

Ilbert, O., Arnouts, S., McCracken, H. J., et al. 2006, A&A, 457, 841

Jakobs, A., Viola, M., McCarthy, I., et al. 2018, MNRAS, 480, 3338

Jing, Y. P. & Suto, Y. 2002, ApJ, 574, 538

Johnston, H., Georgiou, C., Joachimi, B., et al. 2019, Astronomy and Astrophysics, 624, A30

Kannawadi, A., Hoekstra, H., Miller, L., et al. 2019, A&A, 624, A92

Kuijken, K., Heymans, C., Dvornik, A., et al. 2019, A&A, 625, A2

Kuijken, K., Heymans, C., Hildebrandt, H., et al. 2015, MNRAS, 454, 3500

Lange, J. U., van den Bosch, F. C., Hearin, A., et al. 2018, MNRAS, 473, 2830

Law, D. R. & Majewski, S. R. 2010, ApJ, 714, 229

L'Huillier, B., Winther, H. A., Mota, D. F., Park, C., & Kim, J. 2017, MNRAS, 468, 3174

Liske, J., Baldry, I. K., Driver, S. P., et al. 2015, MNRAS, 452, 2087

Mandelbaum, R., Hirata, C. M., Broderick, T., Seljak, U., & Brinkmann, J. 2006, MNRAS, 370, 1008

Melchior, P., Viola, M., Schäfer, B. M., & Bartelmann, M. 2011, MNRAS, 412, 1552

Miller, L., Heymans, C., Kitching, T. D., et al. 2013, MNRAS, 429, 2858

Miller, L., Kitching, T. D., Heymans, C., Heavens, A. F., & van Waerbeke, L. 2007, MNRAS, 382, 315

Napolitano, N. R., Romanowsky, A. J., Capaccioli, M., et al. 2011, MNRAS, 411, 2035

Natarajan, P. & Refregier, A. 2000, ApJ, 538, L113

Navarro, J. F., Frenk, C. S., & White, S. D. M. 1996, ApJ, 462, 563

Nierenberg, A. M., Auger, M. W., Treu, T., Marshall, P. J., & Fassnacht, C. D. 2011, ApJ, 731, 44

O'Brien, J. C., Freeman, K. C., van der Kruit, P. C., & Bosma, A. 2010, A&A, 515, A60

Oguri, M., Bayliss, M. B., Dahle, H., et al. 2012, MNRAS, 420, 3213

Okumura, T., Jing, Y. P., & Li, C. 2009, The Astrophysical Journal, 694, 214

Olling, R. P. 1995, AJ, 110, 591

Parker, L. C., Hoekstra, H., Hudson, M. J., van Waerbeke, L., & Mellier, Y. 2007, ApJ, 669, 21

Peter, A. H. G., Rocha, M., Bullock, J. S., & Kaplinghat, M. 2013, MNRAS, 430, 105

Planck Collaboration, Aghanim, N., Akrami, Y., et al. 2020, A&A, 641, A6

Refregier, A. 2003, MNRAS, 338, 35

Robotham, A. S. G., Norberg, P., Driver, S. P., et al. 2011, MNRAS, 416, 2640

Rozo, E., Rykoff, E. S., Abate, A., et al. 2016, MNRAS, 461, 1431

Sadeh, I., Abdalla, F. B., & Lahav, O. 2016, PASP, 128, 104502

Schrabback, T., Hilbert, S., Hoekstra, H., et al. 2015, MNRAS, 454, 1432

Schrabback, T., Hoekstra, H., Van Waerbeke, L., et al. 2020, arXiv e-prints, arXiv:2010.00311

Shin, T.-h., Clampitt, J., Jain, B., et al. 2018, MNRAS, 475, 2421

Sifón, C., Herbonnet, R., Hoekstra, H., van der Burg, R. F. J., & Viola, M. 2018, MNRAS, 478, 1244

Singh, S., Mandelbaum, R., & More, S. 2015, Monthly Notices of the Royal Astronomical Society, 450, 2195

Springel, V., White, S. D. M., Jenkins, A., et al. 2005, Nature, 435, 629

Taylor, E. N., Hopkins, A. M., Baldry, I. K., et al. 2011, MNRAS, 418, 1587

Tenneti, A., Mandelbaum, R., Di Matteo, T., Feng, Y., & Khandai, N. 2014, MNRAS, 441, 470

Umetsu, K., Sereno, M., Tam, S.-I., et al. 2018, ApJ, 860, 104

Vakili, M., Bilicki, M., Hoekstra, H., et al. 2019, MNRAS, 487, 3715

van de Ven, G., Falcón-Barroso, J., McDermid, R. M., et al. 2010, ApJ, 719, 1481

van Uitert, E., Cacciato, M., Hoekstra, H., et al. 2016, MNRAS, 459, 3251

van Uitert, E., Hoekstra, H., Joachimi, B., et al. 2017, MNRAS, 467, 4131

van Uitert, E., Hoekstra, H., Schrabback, T., et al. 2012, A&A, 545, A71

Velliscig, M., Cacciato, M., Schaye, J., et al. 2015, MNRAS, 453, 721

Vera-Ciro, C. & Helmi, A. 2013, ApJ, 773, L4

Wright, A. H., Robotham, A. S. G., Bourne, N., et al. 2016, MNRAS, 460, 765

Wright, C. O. & Brainerd, T. G. 2000, ApJ, 534, 34

Acknowledgements. The author list is divided into three tiers; the first three authors co-wrote this paper, MB provided infrastructure data as well as made a significant informative contribution to the paper, and the rest of the authors contributed infrastructure and are listed alphabetically. We acknowledge funding from the European Research Council through grant numbers 770935 (AD, HH, AW) and 647112 (CH, BG). HH and AK acknowledges support from Vici grant 639.043.512, financed by the Netherlands Organisation for Scientific Research (NWO). JTAdJ is supported by the NWO through grant 621.016.402. KK acknowledges support by the Alexander von Humboldt Foundation, the Royal Society and Imperial College. MB is supported by the Polish Ministry of Science and Higher Education through grant DIR/WK/2018/12, and by the Polish National Science Center through grants no. 2018/30/E/ST9/00698 and 2018/31/G/ST9/03388. HH is supported by a Heisenberg grant of the Deutsche Forschungsgemeinschaft (Hi 1495/5-1). CH acknowledges support from the Max Planck Society and the Alexander von Humboldt Foundation in the framework of the Max Planck-Humboldt Research Award endowed by the Federal Ministry of Education and Research. HYS acknowledges the support from NSFC of China under grant 11973070, the Shanghai Committee of Science and Technology grant No.19ZR1466600 and Key Research Program of Frontier Sciences, CAS, Grant No. ZDBS-LY-7013. Based on data products from observations made with ESO Telescopes at the La Silla Paranal Observatory under programme IDs 177.A-3016, 177.A-3017 and 177.A-3018, and on data products produced by Target/OmegaCEN, INAF-OACN, INAF-OAPD and the KiDS production team, on behalf of the KiDS consortium. OmegaCEN and the KiDS production team acknowledge support by NOVA and NWO-M grants. Members of INAF-OAPD and INAF-OACN also acknowledge the support from the Department of Physics & Astronomy of the University of Padova, and of the Department of Physics of Univ. Federico II (Naples). GAMA is a joint European-Australasian project based around a spectroscopic campaign using the Anglo-Australian Telescope. The GAMA input catalogue is based on data taken from the Sloan Digital Sky Survey and the UKIRT Infrared Deep Sky Survey. Complementary imaging of the GAMA regions is being obtained by a number of independent survey programmes including GALEX MIS, VST KiDS, VISTA VIKING, WISE, Herschel-ATLAS, GMRT and ASKAP providing UV to radio coverage. GAMA is funded by the STFC (UK), the ARC (Australia), the AAO, and the participating institutions. This work has made use of CosmoHub. CosmoHub has been developed by the Port d'Informació Científica (PIC), maintained through a collaboration of the Institut de Física d'Altes Energies (IFAE) and the Centro de Investigaciones Energéticas, Medioambientales y Tecnológicas (CIEMAT), and was partially funded by the "Plan Estatal de Investigación Científica y Técnica y de Innovación" program of the Spanish government.